

X-ray emission from cosmic web filaments in *SRG/eROSITA* data

H. Tanimura¹, N. Aghanim¹, M. Douspis¹, and N. Malavasi²

¹ Université Paris-Saclay, CNRS, Institut d’Astrophysique Spatiale, Bâtiment 121, 91405 Orsay, France

² Faculty of Physics, Ludwig-Maximilians-Universität, Scheinerstr, Munich, 81679, Germany
e-mail: hideki.tanimura@ias.u-psud.fr

ABSTRACT

Using the publicly available *eROSITA* Final Equatorial Depth Survey (eFEDS) data, we detect the stacked X-ray emissions at the position of 463 filaments at a significance of 3.8σ . The filaments were identified with galaxies in the Sloan Digital Sky Survey survey, ranging from 30 Mpc to 100 Mpc in length at $0.2 < z < 0.6$. The stacking of the filaments is performed with the eFEDS X-ray count-rate maps in the energy range between 0.4 – 2.3 keV after masking the resolved galaxy groups and clusters and the identified X-ray point sources from the *ROSAT*, *Chandra*, *XMM-Newton*, and *eROSITA* observations. In addition, the diffuse X-ray foreground and background emissions are removed by subtracting the signal in the region between 10 – 20 Mpc from the filament spines. For the stacked signal, we perform an X-ray spectral analysis, indicating the signal is associated with a thermal emission. Assuming the plasma emission with the Astrophysical Plasma Emission Code model and a β -model gas distribution with $\beta=2/3$, the detected X-ray signal can be interpreted as an emission from hot gas in the filaments with an average gas temperature of $0.8^{+0.3}_{-0.2}$ keV and a gas overdensity of 41 ± 11 at the center of the filaments.

Key words. cosmology: observations – large-scale structure of Universe – diffuse radiation, X-rays: diffuse background

1. Introduction

In the standard Λ CDM cosmology, more than $\sim 95\%$ of the energy density in the Universe is in the form of dark matter and dark energy, whereas baryonic matter only comprises $\sim 5\%$ (Planck Collaboration 2020). In this model, the structures form via the gravitational collapse of matter in the expanding Universe (e.g., Zeldovich et al. 1982) and result in the large-scale structure of the Universe organized in a web-like pattern called the cosmic web (Bond et al. 1996).

The structure formation has been widely studied with numerical simulations, illustrating that the cosmic web consists of nodes, filaments, sheets, and voids (i.e., Aragón-Calvo et al. 2010b,a; Cautun et al. 2013, 2014). Nodes are dense regions interconnected by filaments and sheets, voids are extremely low-density regions occupying most of the volume in the Universe, and the matter density extends over six orders of magnitude at present (Cautun et al. 2014). In this variety of cosmic environments, baryons are further influenced by radiative cooling and energetic feedback from star formation, supernovae, and active galactic nuclei (AGN), evolving in a complicated manner (Cen & Ostriker 2006; Martizzi et al. 2019; Galárraga-Espinosa et al. 2021b). For example, at high redshifts ($z \gtrsim 2$), most of the expected baryons are found in the Ly α absorption forest: the diffuse, photo-ionized intergalactic medium (IGM) with a temperature of 10^4 – 10^5 K (e.g., Weinberg et al. 1997; Rauch et al. 1997). However, at redshifts $z \lesssim 2$, the observed baryons in stars, the cold interstellar medium, residual Ly α forest gas, OVI, and BLA absorbers, and hot gas in clusters of galaxies account for $\sim 70\%$ of the expected baryons – the remainder has yet to be identified (e.g., Fukugita & Peebles 2004; Shull et al. 2012), these are the so-called “missing baryon”.

Hydrodynamical simulations suggest that 40–50% of baryon could be in the form of shock-heated gas in the cosmic-web filaments between clusters of galaxies (Cen & Ostriker 2006).

This Warm Hot Intergalactic Medium (WHIM) with temperatures ranging between 10^5 and 10^7 K is considered to account for most of the missing baryon (Shull et al. 2012). Therefore, extensive searches for the WHIM have been performed in the far-ultraviolet domain, but also in the X-rays, and thermal Sunyaev-Zel’dovich (tSZ) effect (e.g., Fujita et al. 1996, 2008; Tittley & Henriksen 2001; Dietrich et al. 2005; Werner et al. 2008; Planck Collaboration et al. 2013; Sugawara et al. 2017; Alvarez et al. 2018; Bonjean et al. 2018; Nicastro et al. 2018; Kovács et al. 2019; de Graaff et al. 2019; Tanimura et al. 2019a,b, 2020a,b; Hincks et al. 2022). However, the WHIM is difficult to observe because the signal is relatively weak, and the morphology of the filaments is complex.

The filamentary structure can indeed not be easily identified due to its low density and complicated morphology, therefore, several algorithms have been developed to detect them, such as Spineweb (Aragón-Calvo et al. 2010a), DisPerSE (Sousbie 2011; Sousbie et al. 2011), NEXUS/NEXUS+ (Cautun et al. 2013), Bisous (Tempel et al. 2014), and T-ReX (Bonnaire et al. 2020, 2021). These algorithms have been applied to observational data and identified the filamentary pattern, such as in the distribution of galaxies from the Sloan Digital Sky Survey (Gunn et al. 2006, SDSS) (e.g., Tempel et al. 2014; Chen et al. 2015, 2016; Malavasi et al. 2020; Carrón Duque et al. 2022), the Cosmological Evolution Survey (Scoville et al. 2007, COSMOS) (e.g., Laigle et al. 2018), and VIMOS public extragalactic redshift survey (Scodreggio et al. 2018, VIPERS) (e.g., Malavasi et al. 2017; Moutard et al. 2016a,b). The properties of the filaments were then studied at different wavelengths. For example, Tempel et al. (2014) found that the filaments contain 35 – 40% of the total galaxy luminosity. Chen et al. (2016) showed that galaxies close to filaments are generally brighter than those at significant distance from filaments. Laigle et al. (2018) found that passive galaxies are more confined in the core of the fila-

ment than star-forming ones. Bonjean et al. (2020) unveiled the galaxy distribution and their properties in the SDSS filaments, such as star formation rate, types, stellar mass. Tanimura et al. (2020a) (hereafter T20y) detected the WHIM gas at a significance of $\sim 4\sigma$ with the tSZ effect and at a significance of $\sim 8\sigma$ in the CMB-lensing signal and measured both the gas density and temperature.

In addition more recently, Tanimura et al. (2020b) (hereafter T20x) detected for the first time the X-ray emission from the WHIM gas in large cosmic filaments at a significance of $\sim 4\sigma$ using the *ROSAT* data¹ provided by Snowden et al. (1994) and Snowden et al. (1997). The authors constrained both the gas temperature of $T \sim 0.9^{+1.0}_{-0.6}$ keV and its overdensity of $\delta \sim 30 \pm 15$ at the center of the filaments. They further forecasted the detection of the X-ray emission from filaments in the *SRG/eROSITA* data assuming different sets of gas densities and temperatures. As an extension of T20x work, we use the publicly available *SRG/eROSITA* data in the present study to assess an X-ray emission associated with large cosmic filaments and consequently estimate the gas density and temperature in the filaments. The paper is organised as follows: Section 2 summarizes the datasets used in our analyses. Section 3 explains the stacking method to measure the X-ray emission from filaments. Section 4 presents the model used to interpret our measurements. The possible systematic uncertainties in our measurements are discussed in Section 5. We end the paper with discussion and conclusions in Section 6 and Section 7. Throughout this work, we adopt the Λ CDM cosmology from Planck Collaboration (2020) with $\Omega_m = 0.3158$, $\Omega_b = 0.0494$, and $H_0 = 67.32$ km s⁻¹ Mpc⁻¹. All masses are quoted in solar mass, and M_Δ is mass enclosed within a sphere of radius R_Δ such that the enclosed density is Δ times the *critical* density at redshift z . Uncertainties are given at the 1σ confidence level.

2. Datasets

2.1. eROSITA Final Equatorial Depth Survey

The extended ROentgen Survey with an Imaging Telescope Array (*eROSITA*) (Predehl et al. 2010) is achieving full-sky X-ray surveys with its instrument aboard the Russian Spektrum-Roentgen-Gamma satellite² (SRG). After completing four years of observation, *eROSITA* will achieve eight full-sky surveys, resulting in a sky-averaged exposure time of ~ 2 ks. This will allow the detection of about 100 000 galaxy clusters (SRG/eROSITA Science Book: Merloni et al. 2012).

In the present analysis, we use the *eROSITA* Final Equatorial Depth Survey³ (eFEDS) (Brunner et al. 2021). It has been carried out as a part of the Calibration and Performance Verification (Cal-PV) program between mid-September and mid-December 2019 (about 360 ks, or 100 hours, in total) with all the seven *SRG/eROSITA* Telescope Modules (TM 1-7) in operation. The telescope modules performed scanning observations of ~ 140 square degrees, composed of four individual rectangular raster-scan fields of ~ 35 square degrees each. However, due to an unrecognized malfunction of the camera electronics, 28% of the TM6 data of eFEDS field I and 48% and 43% of the TM5 and TM6 data, respectively, of eFEDS field II could not be used, resulting in a reduced exposure depth in the affected areas of up to $\sim 30\%$. Because the data in these fields have a higher noise

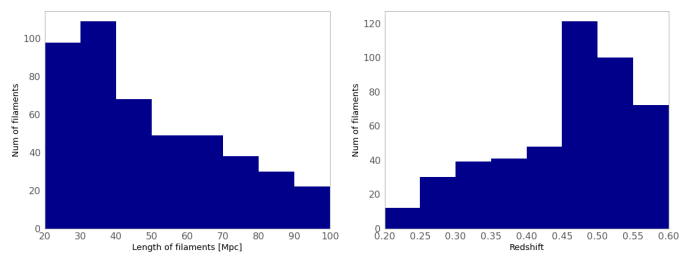


Fig. 1. Length (*left*) and redshift (*right*) distribution of the 463 filaments used in our analysis.

relative to other eFEDS fields, we discard the data in these fields from our analysis.

A set of calibrated data products from *eROSITA*, the Early Data Release (EDR)³, was made public. They consist of calibrated event files with energies between 0.2 - 10 keV and image, exposure, and background maps in the energy range of 0.2 - 0.6 keV, 0.6 - 2.3 keV, and 0.2 - 2.3 keV. EDR also includes the X-ray sources detected at 0.2 - 2.3 keV with a detection likelihood threshold of five. The sources with a detection likelihood larger than six are selected as a main eFEDS catalog (27910 main sources), and the sources with a detection likelihood between five and six are selected as a supplementary eFEDS catalog (4774 supplementary sources). EDR also provides a catalog of 542 galaxy group and cluster candidates, including their position, temperature, luminosity, and flux (Liu et al. 2021). Chiu et al. (2021) estimated the cluster mass calibrated with the weak-lensing data from the Hyper Suprime-Cam (HSC) Subaru Strategic Program survey (Aihara et al. 2018). We aim at detecting and characterizing the X-ray signal in filaments, therefore all these point-like and extended sources are masked in our analysis.

2.2. Filament catalog from SDSS

We use the filament catalog constructed in Malavasi et al. (2020) by applying the Discrete Persistent Structure Extractor (DisPerSE) algorithm (Sousbie 2011) to the LOWZ and CMASS spectroscopic galaxies in the Baryon Oscillation Spectroscopic Survey (BOSS) (Reid et al. 2016). The DisPerSE method computes a gradient of a density field and identifies a critical point where the gradient is zero. The critical point can then be classified as maxima of the density field (e.g. groups or clusters of galaxies), minima of the density field (associated with voids of galaxies), and saddle (local density minima bounded to structures, such as filaments). DisPerSE then defines filaments as field lines of constant gradient that connect critical points (maxima and saddles). In Malavasi et al. (2020), a total of 63,391 filaments were detected, out of which we use 601 filaments with lengths ranging from 30 to 100 Mpc at $0.2 < z < 0.6$ (in order to focus on large cosmic filaments and not on short bridges connecting pairs of clusters, see Galárraga-Espinosa et al. (2021a) for the gas distinction between these two categories) and overlapping with the eFEDS footprint. From the 601 filaments, we finally select 463 filaments in our analysis (see Sect. 3). The length and redshift distribution of the 463 filaments are shown in Fig. 1. The angular size of the filaments' length extends from 0.8 to 6.7 degrees on the sky.

2.3. Point-source and cluster catalogs

In order to remove the contribution from the foreground and background galaxy groups and clusters with lower masses, we

¹ <https://www.jb.man.ac.uk/research/cosmos/rosat/>

² <http://hea.iki.rssi.ru/SRG>

³ <https://erosita.mpe.mpg.de/edr/eROSITAObservations/>

mask the objects from the catalogs listed in T20x. These catalogs include 1653 tSZ clusters from the *Planck* observations (Planck Collaboration 2016) and 1743 MCXC X-ray clusters from the *ROSAT* X-ray survey (Piffaretti et al. 2011) as well as 26 111 redMaPPer clusters (Rykoff et al. 2014), 158 103 WHL clusters (Wen et al. 2012; Wen & Han 2015), and 46 479 AMF clusters (Banerjee et al. 2018) detected from the galaxies in the Sloan Digital Sky Survey (SDSS) survey. The mass and redshift distributions of these objects are shown in Tanimura et al. (2019a), and the mass distribution in the union catalog reaches down to $\sim 3 \times 10^{13} M_{\odot}$. We mask all these groups and clusters of galaxies from the union catalog that fall in the eFEDS footprint. In addition, as mentioned in Sect. 2.1, we mask the 542 galaxy clusters detected directly in the eFEDS observation.

Moreover, we mask the X-ray point sources detected in the *ROSAT*, *Chandra*, and *XMM-Newton* observations. These include 135 118 point-like sources in the Second *ROSAT* All-Sky Survey Point Source Catalog (2RXS)⁴ (Boller et al. 2016), 317 167 X-ray sources in the *Chandra* Source Catalog (CSC 2.0)⁵ (Evans et al. 2010), and 775 153 sources in the third generation catalog of X-ray sources from *XMM-Newton* observatory (3XMM-DR8)⁶ (Rosen et al. 2016). Here again, we mask all these X-ray point sources that fall in the eFEDS footprint, in addition to those detected in EDR.

3. Stacking analysis

This section describes the procedure by which we stack the eFEDS maps at the position of the cosmic filaments. We then estimate the X-ray signal associated with the filaments. For the stacking method, we follow the procedure initiated in T20y and optimized for the X-ray data in T20x.

3.1. Masking clusters and point sources

Before stacking the X-ray eFEDS maps, we mask out all the sources listed in Sect. 2. The point sources are masked by a radius of 30 arcsec, much larger than the angular resolution of *SRG/eROSITA* that has an on-axis angular resolution of 5.7 – 9.3 arcsec in FWHM, depending on the detector (TM 1–7) (Predehl et al. 2021). The galaxy groups and clusters are masked by $3 \times R_{500}$, corresponding to about 1.5 times their virial radius. In addition, we mask the maxima of the galaxy density field identified by DisPerSE, which are possible locations of unresolved galaxy clusters. We mask these maxima by a radius of 30 arcsec. We do not mask other critical points identified by DisPerSE, such as minima and saddle, because they are associated with low-density regions. We checked that our results do not change by varying these mask sizes, as shown later in Sect. 5. As a result of this masking procedure and of the removal of the low-exposure eFEDS fields, where the noise is higher (see Sect. 2), the available eFEDS area for our stacking analysis corresponds to $\sim 32\%$ of the initial eFEDS observed area.

3.2. Stacking method

We use the eFEDS image and exposure maps at 0.2 - 0.6 keV and 0.6 - 2.3 keV provided in EDR. We compute the count rate of the X-ray photons in the eFEDS field and stack the count-rate map at the position of the filaments. We do not use the provided eFEDS

background maps in our analysis because our analysis pipeline includes a background-subtraction step. We have checked that subtracting the background maps from the image maps does not change our results.

Then, we follow the stacking method in T20x that is illustrated in Fig. 2. (i) In the left panel of Fig. 2, the black dots represent the extremities of the segments, defining the filament by DisPerSE. The black straight line connecting these extremities constitute the filament spine. We use data within 20 Mpc from the filament spine. For each data point within the 20 Mpc, the closest distance to the filament spine is computed. Then, the data are divided into eight distance bins up to 20 Mpc, as illustrated in Fig. 3, and the average value of the count rate in each distance bin is computed. From the extent of the data profile in Fig. 3, data within 10 Mpc from the filament spine are used to estimate the S/N of our measurement shown in light gray, and those between 10 – 20 Mpc are used for our background estimate, described below in the step (iii), shown in dark gray.

(ii) In the left panel of Fig. 2, white disks are the masked regions; data in these regions are not used in our analysis. A filament may be largely masked if it is located close to our excluded area or massive clusters in the foreground or background (see Sect. 3.1). In this extreme situation, we discard the filament if the resulting radial profile has empty radial bins (i.e., no data are accumulated in the bins because of the masking procedure). This process reduces the number of SDSS filaments in the eFEDS region from 601 to 473 at 0.2 - 0.6 keV and to 463 at 0.6 - 2.3 keV. (Two effects cause the lower number of available filaments at 0.6 - 2.3 keV: empty bins due to the masking procedure and empty bins due to the lower number of X-ray photons at higher energies than those at lower energies.) In our analysis, we use the commonly selected 463 filaments.

(iii) To estimate the excess of the X-ray signal associated with the filament, we subtract the average signal in the outskirts in a region covering 10–20 Mpc from the filament spine defined as the local background signal. It corresponds to the dark gray area in the left panel in Fig. 2. This subtraction mitigates the contamination from both the foreground and background emissions, such as the diffuse Galactic and extragalactic emissions.

(iv) Steps (i)–(iii) are repeated for all the usable filaments, and the ensemble of background-subtracted radial profiles is obtained. To account for the mask effect that does not impact each filament in the same manner, we compute the weighted average of the background-subtracted radial profiles. The weight is calculated as a ratio of the unmasked area to the total area. The resulting weighted average profile is then given by

$$\bar{x}(r) = \frac{\sum w_i (x_i(r) - x_{i,bg})}{\sum w_i} \left(w_i = \frac{A_{i,unmask}}{A_{i,total}} \right), \quad (1)$$

where $x_i(r)$ is the X-ray count-rate radial profile of the i -th filament, $x_{i,bg}$ is the average signal at 10–20 Mpc from the i -th filament's spine, $A_{i,total}$ is the total area and $A_{i,unmask}$ is the unmasked area within 20 Mpc from the i -th filament's spine.

3.3. Results

Following the stacking method described above, we first analyzed the sample of 463 filaments using the eFEDS count-rate map at 0.2 – 0.6 keV. The resulting stacked radial profile is shown in black in the left panel of Fig. 3. We then assessed the uncertainty of the profile by bootstrap resampling, also by following the procedure in T20x, in which we drew a random sampling of 463 filaments with replacements and recalculated

⁴ <http://www.mpe.mpg.de/ROSAT/2RXS>

⁵ <http://cxc.cfa.harvard.edu/csc2/>

⁶ <https://www.cosmos.esa.int/web/xmm-newton/xsa#download>

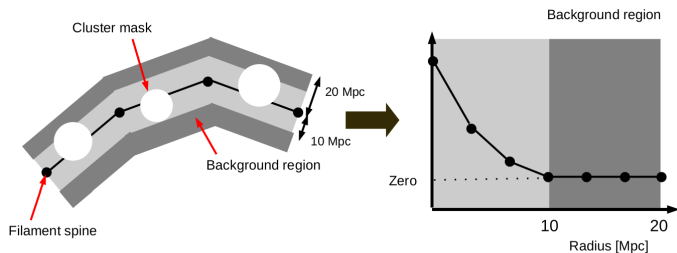


Fig. 2. Illustration to compute a radial profile of one filament. In the left panel, black dots are the extremities of the segments of filament given by DisPerSE. The black straight line connecting these extremities constitutes the filament spine. The light and dark gray area is the area within a physical distance up to 20 Mpc from the filament spine, and this area is used to compute a radial profile of the filament, as shown in the right panel. The dark gray area is the area within a physical distance of 10–20 Mpc from the filament spine, defined as a background region. The average signal in the background region is subtracted from the radial profile. White disks are masked regions excluded from our analysis.

the stacked profile for the new combination of 463 filaments. We repeated this process 1000 times and produced 1000 stacked profiles. Finally, we computed the standard deviation of this ensemble and used it as the one σ uncertainty of our measurement, which is shown as the gray region in Fig. 3. As shown in the figure, our measurement at 0.2 – 0.6 keV is consistent with zero. This is expected from the results of T20x, who stacked the *ROSAT* maps at the position of 15 165 filaments but did not find a signal excess below 0.56 keV. The reason is likely because at the low energy bands, the background signal starts to dominate over the filament signal, as shown in the predicted spectra in T20x. We next analyzed the sample of 463 filaments using the eFEDS count-rate maps at 0.6 – 2.3 in the same manner and found an excess signal as shown in the right panel of Fig. 3.

In order to assess the *rms* fluctuation due to the foreground and background X-ray emissions in the unmasked regions, we performed a null test based on a Monte Carlo method, as conducted in T20x. In the null test, we replaced each of the 463 filaments at random positions on the eFEDS field and then stacked the X-ray count-rate map at the new positions of the 463 filaments. We repeated this null test 1000 times and computed the average and standard deviation of the 1000 null-test set of profiles. The result shows that the average of the null profiles is consistent with zero with no discernible structure, as shown in Fig. 3. This result suggests that our estimator is not biased by the foreground and background X-ray emissions. In addition, the standard deviation of the null profiles is consistent with the uncertainty from the bootstrap estimate (gray area in Fig. 3), and the ensemble of the null profiles can be used to estimate the uncertainty and significance of our measured signal.

We hence estimate the signal-to-noise ratio (S/N) of our measured X-ray profile as

$$S/N = \sqrt{\chi_{\text{data}}^2 - \chi_{\text{null}}^2}, \quad (2)$$

where

$$\chi_{\text{data}}^2 = \sum_{i,j} x_{\text{data}}(R_i)^T (C_{ij}^{-1}) x_{\text{data}}(R_j) \quad (3)$$

$$\chi_{\text{null}}^2 = \sum_{i,j} x_{\text{null}}(R_i)^T (C_{ij}^{-1}) x_{\text{null}}(R_j), \quad (4)$$

where $x_{\text{data}}(R_i)$ is the X-ray count-rate at the R_i bin from the data X-ray profile, $x_{\text{null}}(R_i)$ is the value at the R_i bin from the null

tests, and C_{ij} is the covariance matrix of the data X-ray profile, estimated from bootstrap resampling. The S/N value was estimated to be ~ 0.9 at 0.2 – 0.6 keV and ~ 2.8 at 0.6 – 2.3 keV using the data points up to 10 Mpc, determined from the extent of the data profile. The possible sources of systematic effects will be discussed in Sect. 5

4. Physical interpretation

In this section, we perform an X-ray spectral analysis for our measurements based on physical models, and we derive the gas density and temperature in the filaments. As performed in T20x, our analysis focuses on the core of the filaments because the S/N of our measurements is low at the outskirts, and it does not allow us to determine the physical properties at the outskirts. The size of the filament core is set to ~ 2.5 Mpc based on the temperature profile of filaments from hydrodynamic simulations (Galárraga-Espinosa et al. 2021a), in which the authors show a flat temperature profile from the center to ~ 2.5 Mpc.

4.1. Spectral energy distribution

To perform our X-ray spectral analysis, we produced new image maps with narrower energy bands using the eROSITA Science Analysis Software System (eSASS) developed by the eROSITA collaboration. The eSASS includes a collection of tasks, scripts, and libraries to create eROSITA calibrated science data products and to perform various interactive data analysis tasks (Brunner et al. 2021; Predehl et al. 2021).

As processed in Brunner et al. (2021), using the *evtool* command in the eSASS software, we merged the four event files into one, applied filters of FLAG = 0xc00fff30 (select good events from nominal field of view, excluding bad pixels), PATTERN ≤ 15 (include single, double, triple, and quadruple events), and FLAREGTI (background flare is filtered out), extracted the selected events in specific energy ranges, and created image maps with a resolution of 4 arcsec per pixel. We did not correct the data from the temporary malfunctioning of the camera electronics. Instead, we masked the associated area including these data. We created image maps in the energy range of 0.4 – 0.5, 0.5 – 0.6, 0.6 – 0.8, 0.8 – 1.0, 1.0 – 1.3, and 1.3 – 2.3 keV. These energy bins were determined to increase the number of energy bands and for the total number of X-ray photons not to be low at each energy band. We excluded the X-ray events below 0.4 keV and above 2.3 keV because the S/N at those energy bands are consistent with zero, and adding these data did not change our results. From these new image maps, we re-computed the count-rate maps.

Before proceeding to the stacking analysis for the new count-rate maps, we additionally masked the overlap area of filaments at different redshifts in $0.2 < z < 0.6$, as performed in T20x. This masking step avoids accumulating X-ray signals from possible overlapping filaments in the same line of sight and thus gives a conservative X-ray signal for our filament sample. The mask size is 5 arcmin, corresponding to the average angular core size of our filament sample. After full masking procedure, we repeated our stacking analysis on the new count-rate maps at the six energy bands and computed the X-ray count-rate profiles. From these profiles, we extracted the average X-ray signals within 2.5 Mpc at the cores of the filaments and obtained the spectral energy distribution (SED) of the X-ray signal, which is shown in black in Fig. 4. We estimated the S/N of the SED measurement at 0.4 – 2.3 keV using the covariance matrix from the 463 filaments and

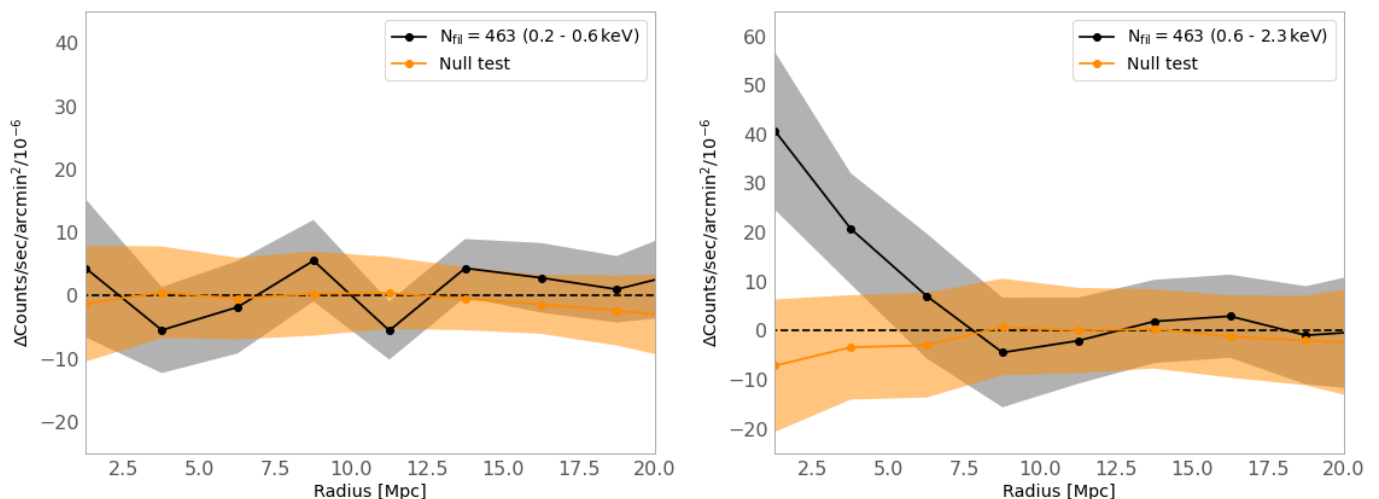


Fig. 3. Black: Average radial X-ray profile of the 463 filaments at 0.2 – 0.6 keV (left) and 0.6 – 2.3 keV (right). The 1σ uncertainty is estimated by a bootstrap resampling, shown as a width of gray area. Orange: Average radial X-ray profile from 1000 null-test profiles. In the null test, each of the 463 filaments is displaced at random positions in the eFEDS field and then stacked. This procedure is repeated 1000 times, producing 1000 null-test profiles. The 1σ uncertainty is estimated by a standard deviation of the 1000 null-test profiles.

found it to be 3.8, computed from the excesses at the six energy bands.

T20x predicted the S/N of the X-ray emission from stacked filaments relative to the background with different sets of gas densities and temperatures for *SRG/eROSITA*. In Fig. 4 of T20x, a detection at $\sim 10\sigma$ is predicted for ~ 463 stacked filaments with $T \sim 0.9$ keV and $\delta \sim 30$. This forecast was obtained by stacking the filaments from the brightest to the dimmest, whereas in the present analysis, the filaments used are not the brightest 463 ones, but they include bright, mildly-bright, and dim filaments. Following T20x, we thus re-computed the S/N, corresponding to our 463 filaments, the obtained S/N is estimated to be ~ 4.1 in very good agreement with our present result of S/N ~ 3.8 .

4.2. Model fitting

As with T20x, we model the X-ray SED measurement using the Python X-ray spectral analysis package (PyXspec) interface with the X-ray spectral analysis package (XSPEC) (Arnaud 1996) with the response file, “erosita_iv_7telfov_ff.rsp”⁷. We consider the X-ray emission based on the Astrophysical Plasma Emission Code (APEC) model (Smith et al. 2001) with two free parameters: the normalization of surface brightness and temperature. We assume the gas metallicity to be ~ 0.1 of the solar value (Anders & Grevesse 1989) based on the filament analysis with the IllustrisTNG simulations (private communication with Galárraga-Espinosa et al. 2021a). The neutral atomic hydrogen (HI) column density in the eFEDS region is estimated to be $\sim 3 \times 10^{20} \text{ cm}^2$ with the HI4PI map (HI4PI Collaboration et al. 2016). We use the median redshift of the 463 filaments, $z \sim 0.48$, for the fitting.

We fitted this APEC model to the data with a minimum chi-square method (see Fig. 4) and obtained a surface brightness of $(0.13 \pm 0.03) \times 10^{-12} \text{ erg cm}^{-2} \text{ s}^{-1} \text{ deg}^{-2}$ at 0.5–2.0 keV and a gas temperature of $0.8_{-0.2}^{+0.3}$ keV. The reduced χ^2 value was 0.8.

The surface brightness is a projected X-ray emission from the gas in filaments and can be converted to a gas density given a density distribution model. While the gas distribution in filaments is not well known, it was studied using the tSZ measure-

ments in T20y, in which the authors showed that a cylindrical filament with a β -model (Cavaliere & Fusco-Femiano 1978) with $\beta=2/3$ fitted the data well. Thus, we use their model for the gas distribution in filaments.

The gas distribution in the β model is given by

$$n_e(r, z) = \frac{n_{e,0}(z)}{1 + (r/r_{e,c})^2} \quad \text{in } r < R_{\text{fil}} \quad (5)$$

where $n_{e,0}(z)$ is the central electron density of a filament at redshift z , r is the radius, and $r_{e,c}$ is the core radius of the electron distribution, and R_{fil} is the cutoff radius. We set $r_{e,c} = 1.5$ Mpc and $R_{\text{fil}} = 10$ Mpc found in T20y. As with T20x, we assume a negligible evolution of overdensity in filaments in the redshift range of our filament sample at $0.2 < z < 0.6$ and use a central electron overdensity $\delta_{e,0}$ as a free parameter. Then, the electron density of a filament at redshift z is given by

$$n_{e,0}(z) = \frac{n_{e,0}(z)}{\bar{n}_e(z)} \bar{n}_e(z) = (1 + \delta_{e,0}) \bar{n}_e(z=0) (1+z)^3, \quad (6)$$

where $\bar{n}_e(z)$ is the mean electron density at redshift z in the Universe. We also included an orientation angle of a filament on the plane of the sky in our model because the amplitude of surface brightness depends on it. The orientation angle of a filament was computed from the 3-dimensional position of a filament spine in our filament catalog. With this model, the average gas overdensity at the center of the 463 filaments was estimated to be 41 ± 11 .

We also consider a simple density model: a cylindrical filament with a constant density, given by

$$n_e(r, z) = n_{e,0}(z) \quad \text{in } r < R_{\text{fil}} \quad (\text{constant density model}), \quad (7)$$

where R_{fil} is set to be 5 Mpc as in T20y. With this model, the average gas overdensity in the 463 filaments was estimated to be 10 ± 3 .

5. Systematic effects

Possible bias in our stacked X-ray signals may be caused by residual contamination from foreground or background galaxy

⁷ <http://www2011.mpe.mpg.de/erosita/response/>

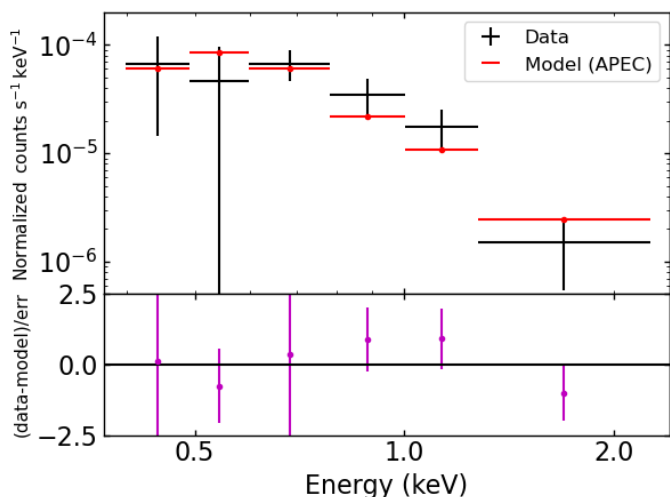


Fig. 4. (Top panel) Black: Excesses of X-ray emission at the core of the 463 filaments (< 2.5 Mpc from the filament spines), relative to the background (average X-ray signal at $10\text{--}20$ Mpc from the filament spines) at the six energy bands. The 1σ uncertainties are estimated by a bootstrap resampling. Red: The fit to the data with the APEC model (see text for details). (Bottom panel) Magenta: Ratio of data and model at each energy band.

clusters. In order to check this, we varied the radius of the circular mask associated with clusters in the range of $[0 - 3] \times R_{500}$. As demonstrated in the upper panel of Fig. 5, the result do not show any significant difference in the X-ray profiles when the clusters are masked by more than $1 \times R_{500}$. This shows that our conservative choice of a $3 \times R_{500}$ mask for the clusters makes their contribution to our measured signal quite negligible. A bias may also be induced by the contamination from point sources, such as AGN. To check this, we varied the radius of the source mask in the range of $[0 - 45]$ arcsec. The result is shown in the lower panel of Fig. 5. We do not see any significant difference in the X-ray profiles when the point sources were masked by a size larger than 30 arcsec, showing that the point sources are well masked with our applied mask size of 30 arcsec.

The unresolved cosmic X-ray background (CXB) may also contribute to the signal, but this contribution is handled by the background subtraction procedure, which removes local foreground and background signals around each filament. Including this procedure, we indeed find that the null-test profiles are consistent with zero, indicating that the results are not biased by residual contamination from unresolved AGN and low-mass galaxy groups (Kolodzig et al. 2017). The background subtraction procedure also removes the diffuse Galactic emission, which is proved by the flat null-test profiles at the low energy band of $0.2 - 0.6$ keV in Fig. 3.

We additionally checked whether a non-thermal emission could fully explain the detected signals. To check it, we fitted our X-ray SED measurements with a power-law model with normalization and photon index as two free parameters. We found the model fits better the data, with the reduced χ^2 value of 1.1 instead of 0.8 with the APEC model. However in this model, the photon index is found to be ~ 3.7 , which is extremely steep compared to the expected value for the AGNs of ~ 2 (e.g., Ishibashi & Courvoisier 2010; Yang et al. 2015) and to the one for the CXB of $1.42 - 1.74$ (e.g., Lumb et al. 2002; De Luca & Molendi 2004; Kolodzig et al. 2017). If we fit the data with a power-law model

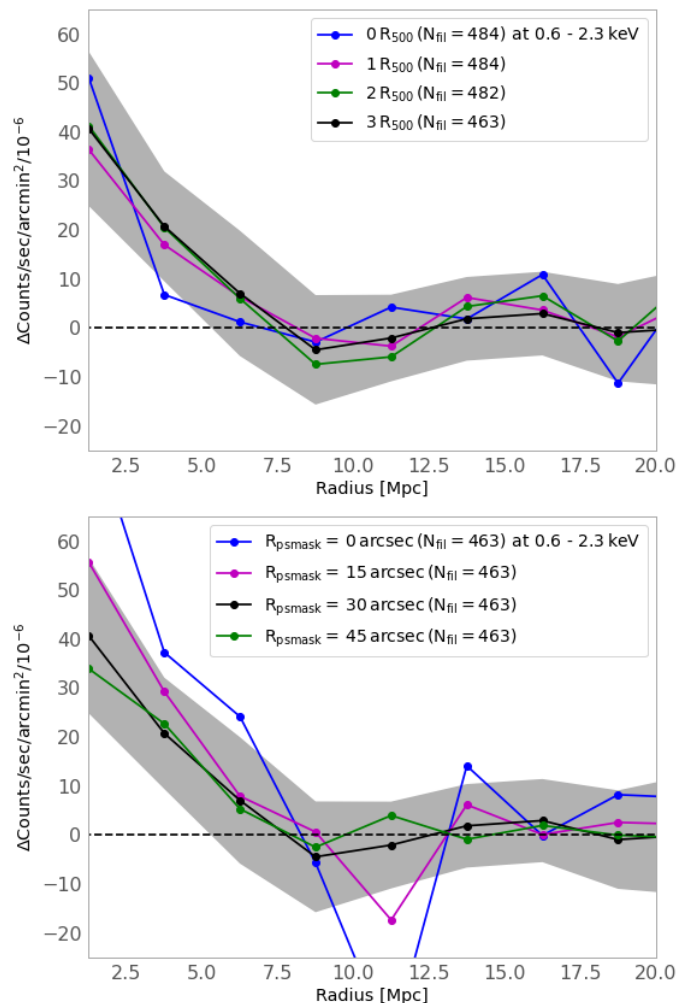


Fig. 5. Upper: Average radial X-ray profiles of filaments at $0.6 - 2.3$ keV with different sizes for the cluster masks: No cluster mask (blue), $1 \times R_{500}$ (magenta), $2 \times R_{500}$ (green), and $3 \times R_{500}$ (black). Lower: Average radial X-ray profiles of filaments at $0.6 - 2.3$ keV with different sizes for the point-source masks: No mask (blue), 15 arcsec (magenta), 30 arcsec (black), and 45 arcsec (green).

using these realistic photon-index values, the reduced χ^2 value is worsened to $\sim 3.0 - 3.7$ (~ 3.0 for the photon index of 2.0 and ~ 3.7 for the photon index of 1.42). This test suggests that our detected signals cannot be explained only by a non-thermal emission. To further check the possible contribution to our detected signal from a non-thermal component, we fitted our data with a two-component model: APEC and power-law with the photon index in the range of $1.42 - 2.0$. The result of the fitting shows that the contribution of the power-law component is less than $\sim 1.4 \times 10^{-16}$ erg cm $^{-2}$ s $^{-1}$ deg $^{-2}$ ($0.5\text{--}2.0$ keV) compared to $\sim 1, 3 \times 10^{-13}$ erg cm $^{-2}$ s $^{-1}$ deg $^{-2}$ ($0.5\text{--}2.0$ keV) of the APEC component. We thus found that the contribution from a non-thermal origin in our measurements is very minor, three orders of magnitudes smaller, relative to that of a thermal origin.

While we assumed a metallicity of $0.1Z_{\odot}$, the metallicity measurements in peripheries of ICM (Mernier et al. 2017, 2018) show the value of $\sim 0.2Z_{\odot}$. Therefore, we repeated our spectral analysis with $0.2Z_{\odot}$. Then, the average gas temperature in the filament cores was estimated to be ~ 0.9 keV and the surface brightness to be $\sim 0.12 \times 10^{-12}$ erg cm $^{-2}$ s $^{-1}$ deg $^{-2}$ ($0.5\text{--}2.0$

keV). These values are within the uncertainties of our measurements for $0.1Z_{\odot}$, suggesting no significant bias in our results.

Finally, we checked whether the fitting of all stacked profiles with a single redshift could impact our final results. To do so, we performed the model fitting with four APEC models with redshifts of 0.25, 0.35, 0.45, and 0.55 by linking their plasma temperatures and normalizations, in which the normalizations were weighted by the relative number of filaments in each redshift bin. The resulting temperature and surface brightness were estimated to be ~ 0.80 keV and $\sim 0.11 \times 10^{-12}$ erg cm $^{-2}$ s $^{-1}$ deg $^{-2}$ (0.5–2.0 keV), respectively. These values are $\sim 5\%$ and $\sim 10\%$ lower than the values estimated with a single redshift but still within our measurement uncertainties.

6. Discussion

While most of the actual measurements for gas in filaments are still limited to short filaments with lengths smaller than ~ 10 Mpc in the cluster outskirts (e.g., Eckert et al. 2015; Hattori et al. 2017) or between galaxy clusters (e.g., Epps & Hudson 2017; Alvarez et al. 2018; Bonjean et al. 2018; Tanimura et al. 2019a,b; de Graaff et al. 2019; Hincks et al. 2022), T20x and T20y reported X-ray and tSZ measurements from the cosmic filaments with the lengths of 30–100 Mpc using the *ROSAT* X-ray data and the *Planck* tSZ data, respectively. In their studies, the gas overdensity at the core of filaments was estimated to be $\delta = 30 \pm 15$ in T20x and $\delta = 19.0^{+27.3}_{-12.1}$ in T20y, assuming the β -model. These values are consistent with our present results of $\delta = 41 \pm 11$.

Ursino & Galeazzi (2006) predicted in their simulations that the WHIM contribution in the total diffuse X-ray background might reach up to 20% in 0.37–0.925 keV, most of which originating from filaments at redshifts between 0.1 and 0.6. The detected signal from our sample of filaments at $0.2 < z < 0.6$ peaks at ~ 0.7 keV, as shown in Fig. 4, consistent with these predictions. The gas temperature was estimated to be $0.9^{+1.0}_{-0.6}$ keV in T20x, which is consistent with our result of $0.8^{+0.3}_{-0.2}$ keV. The uncertainty of the temperature estimate is significantly improved by a factor of 2–3 relative to that in T20x. Given the similar level of S/N between these two measurements, this improvement is likely attributed to the improved energy resolution and the extended energy range of *SRG/eROSITA* with respect to *ROSAT*.

However, by contrast, the gas temperature estimated in T20y (0.12 ± 0.03 keV) is relatively lower than our result and that in T20x. The difference may be caused by the fact that the gas temperatures in our study and in T20x are estimated at the filament core ($< \sim 2.5$ Mpc), whereas the value in T20y is the average within 5 Mpc. This temperature difference may imply a radial gradient of the gas temperature: hotter at the core compared to the outskirts. Such a radial gradient of the gas temperature in filaments is predicted by hydrodynamic simulations in Gheller & Vazza (2019), in which the authors show that the gas temperature is constant up to ~ 2.5 Mpc from the filament core with a temperature of $\sim 3 \times 10^6$ K (~ 0.3 keV) and starts to drop beyond this distance. The gas temperature profile in filaments is also predicted with the IllustrisTNG simulations in Galárraga-Espinosa et al. (2021a). The authors show that the gas temperature profile of different lengths of filaments is constant up to ~ 2.5 Mpc from the filament core with a temperature of $(0.5\text{--}2.0) \times 10^6$ K ($\sim 0.05\text{--}2$ keV), depending on the filament length, and quickly drops to

$\sim 1.0 \times 10^5$ K (~ 0.01 keV) at 20 Mpc from the filament core. Thus, the gas temperature gradient is predicted in hydrodynamic simulations, but our estimated gas temperature is higher than the predictions from hydrodynamic simulations. The reasons of this difference is still not clear due to relatively large uncertainties of our temperature measurements, but future *SRG/eROSITA* data will provide an all-sky X-ray measurement that will help understanding in more details the physical properties of gas in filaments.

7. Conclusions

We selected 463 filaments overlapping with the eFEDS field, at $0.2 < z < 0.6$ ranging from 30 Mpc to 100 Mpc in length, identified in the SDSS survey. We stacked the eFEDS' count-rate maps around these filaments, excluding resolved galaxy groups and clusters as well as the detected X-ray point sources from the *ROSAT*, *Chandra*, *XMM-Newton*, and *eROSITA* observations. In our stacking analysis, the average signal in the local background region, 10 to 20 Mpc from the filament spine, was subtracted in order to remove the diffuse Galactic and extragalactic emissions.

We detected an X-ray excess signal from the stacking of the filaments in the EDR count-rate maps at 0.6–2.3 keV, provided by the *eROSITA* collaboration, at a significance of 2.8σ . In order to perform a spectral analysis, we defined six energy bands, 0.4–0.5, 0.5–0.6, 0.6–0.8, 0.8–1.0, 1.0–1.3, and 1.3–2.3 keV, and constructed the associated count-rate maps using the calibrated event files provided in EDR. We then repeated our stacking analysis at each energy band, extracted the X-ray signal at the core of the filaments within 2.5 Mpc, and obtained the SED measurement of the X-ray signals. The S/N of the SED measurement was estimated to be 3.8, computed from the excesses at the six energy bands.

For the physical interpretation of the detected X-ray excess signal, we performed a spectral analysis of the SED measurement. The detected signal cannot be explained by a non-thermal emission. Indeed, if we fit our measurement with a power-law model using realistic photon-index values in the range of 1.4–2.0 for X-ray emissions from AGN or CXB, the reduced χ^2 value is $\sim 3.0\text{--}3.7$ compared to the reduced χ^2 of 0.8 when we fit with the APEC model assuming a thermal origin. Moreover, if we fit our data with a two-component model: APEC and power-law with the photon index in the range 1.4–2.0, the result shows that the contribution of the power-law component is much lower than that of the APEC component by about three orders of magnitude. These results support the fact that our detected signal has a thermal origin and can not be explained by a non-thermal origin.

We fitted our measurement, assuming the APEC model for the thermal emission. This provided a surface brightness of $(0.13 \pm 0.03) \times 10^{-12}$ erg cm $^{-2}$ s $^{-1}$ deg $^{-2}$ at 0.5–2.0 keV and a gas temperature of $0.8^{+0.3}_{-0.2}$ keV with the reduced χ^2 value of 0.8. This surface brightness corresponds to a gas overdensity of 41 ± 11 at the center of the filaments assuming the gas distribution in filaments with a β -model with $\beta = 2/3$ or 10 ± 3 assuming a constant gas distribution within 5 Mpc from the filament spines.

The origin of the thermal emission associated with the X-ray signal is still not clear. In our analysis, the known galaxy groups

and cluster with the masses above $\sim 3 \times 10^{13} M_{\odot}$ are masked. Thus, the possible explanations for the thermal emission are either low-mass halos with masses below $\sim 3 \times 10^{13} M_{\odot}$ or diffuse gas in the filaments. To distinguish between these contributions, the gas distribution around the low-mass halos needs to be understood; however, it is not well constrained so far. For example, the gas fraction in low-mass halos does not agree among different hydrodynamic simulations (e.g., Chisari et al. 2018; Schneider et al. 2019). To interpret the nature of the thermal emission measure in stacked filaments, *SRG/eROSITA* will provide an all-sky X-ray measurement, and the data will help to understand the gas distribution around low-mass halos. As another probe for the gas distribution around halos, the kinetic SZ (kSZ) effect from *Planck* and ACT observations can be used, as shown in Amodeo et al. (2021); Schaan et al. (2021); Tanimura et al. (2021, 2022). Current sensitivity of the kSZ measurements requires a large number of stacked objects to obtain the halo's gas distribution and does not allow to study their mass and redshift dependence. However, the upcoming Simons Observatory (Simons Observatory Collaboration 2019) and CMB-S4 (Abazajian et al. 2016) with a better sensitivity will allow us to study them and clarify the origin of the thermal emission from the cosmic filaments.

Acknowledgements. This research has been supported by the funding for the Baryon Picture of the Cosmos (ByoPiC) project from the European Research Council (ERC) under the European Union's Horizon 2020 research and innovation programme grant agreement ERC-2015-AdG 695561. The authors acknowledge fruitful discussions with the members of the ByoPiC project (<https://byopic.eu/team>). This work is based on data from *eROSITA*, the soft X-ray instrument aboard SRG, a joint Russian-German science mission supported by the Russian Space Agency (Roskosmos), in the interests of the Russian Academy of Sciences represented by its Space Research Institute (IKI), and the Deutsches Zentrum für Luft- und Raumfahrt (DLR). The SRG spacecraft was built by Lavochkin Association (NPOL) and its subcontractors, and is operated by NPOL with support from the Max Planck Institute for Extraterrestrial Physics (MPE). The development and construction of the *eROSITA* X-ray instrument was led by MPE, with contributions from the Dr. Karl Remeis Observatory Bamberg & ECAP (FAU Erlangen-Nuernberg), the University of Hamburg Observatory, the Leibniz Institute for Astrophysics Potsdam (AIP), and the Institute for Astronomy and Astrophysics of the University of Tübingen, with the support of DLR and the Max Planck Society. The Argelander Institute for Astronomy of the University of Bonn and the Ludwig Maximilians Universität Munich also participated in the science preparation for *eROSITA*. The *eROSITA* data shown here were processed using the eSASS software system developed by the German *eROSITA* consortium.

References

Abazajian, K. N., Adshead, P., Ahmed, Z., et al. 2016, arXiv e-prints, arXiv:1610.02743

Aihara, H., Arimoto, N., Armstrong, R., et al. 2018, PASJ, 70, S4

Alvarez, G. E., Randall, S. W., Bourdin, H., Jones, C., & Holley-Bockelmann, K. 2018, ApJ, 858, 44

Amodeo, S., Battaglia, N., Schaan, E., et al. 2021, Phys. Rev. D, 103, 063514

Anders, E. & Grevesse, N. 1989, Geochim. Cosmochim. Acta, 53, 197

Aragón-Calvo, M. A., Platen, E., van de Weygaert, R., & Szalay, A. S. 2010a, ApJ, 723, 364

Aragón-Calvo, M. A., van de Weygaert, R., & Jones, B. J. T. 2010b, MNRAS, 408, 2163

Arnaud, K. A. 1996, in Astronomical Society of the Pacific Conference Series, Vol. 101, Astronomical Data Analysis Software and Systems V, ed. G. H. Jacoby & J. Barnes, 17

Banerjee, P., Szabo, T., Pierpaoli, E., et al. 2018, New A, 58, 61

Boller, T., Freyberg, M. J., Trümper, J., et al. 2016, A&A, 588, A103

Bond, J. R., Kofman, L., & Pogosyan, D. 1996, Nature, 380, 603

Bonjean, V., Aghanim, N., Douspis, M., Malavasi, N., & Tanimura, H. 2020, A&A, 638, A75

Bonjean, V., Aghanim, N., Salomé, P., Douspis, M., & Beelen, A. 2018, A&A, 609, A49

Bonnaire, T., Aghanim, N., Decelle, A., & Douspis, M. 2020, A&A, 637, A18

Bonnaire, T., Aghanim, N., Kuruvilla, J., & Decelle, A. 2021, arXiv e-prints, arXiv:2112.03926

Brunner, H., Liu, T., Lamer, G., et al. 2021, arXiv e-prints, arXiv:2106.14517

Carrón Duque, J., Migliaccio, M., Marinucci, D., & Vittorio, N. 2022, A&A, 659, A166

Cautun, M., van de Weygaert, R., & Jones, B. J. T. 2013, MNRAS, 429, 1286

Cautun, M., van de Weygaert, R., Jones, B. J. T., & Frenk, C. S. 2014, MNRAS, 441, 2923

Cavaliere, A. & Fusco-Femiano, R. 1978, A&A, 70, 677

Cen, R. & Ostriker, J. P. 2006, ApJ, 650, 560

Chen, Y.-C., Ho, S., Brinkmann, J., et al. 2016, MNRAS, 461, 3896

Chen, Y.-C., Ho, S., Freeman, P. E., Genovese, C. R., & Wasserman, L. 2015, MNRAS, 454, 1140

Chisari, N. E., Richardson, M. L. A., Devriendt, J., et al. 2018, MNRAS, 480, 3962

Chiu, I.-N., Ghirardini, V., Liu, A., et al. 2021, arXiv e-prints, arXiv:2107.05652

de Graaff, A., Cai, Y.-C., Heymans, C., & Peacock, J. A. 2019, A&A, 624, A48

De Luca, A. & Molendi, S. 2004, A&A, 419, 837

Dietrich, J. P., Schneider, P., Clowe, D., Romano-Díaz, E., & Kerp, J. 2005, A&A, 440, 453

Eckert, D., Jauzac, M., Shan, H., et al. 2015, Nature, 528, 105

Epps, S. D. & Hudson, M. J. 2017, MNRAS, 468, 2605

Evans, I. N., Primini, F. A., Glotfelty, K. J., et al. 2010, ApJS, 189, 37

Fujita, Y., Koyama, K., Tsuru, T., & Matsumoto, H. 1996, PASJ, 48, 191

Fujita, Y., Tawa, N., Hayashida, K., et al. 2008, PASJ, 60, S343

Fukugita, M. & Peebles, P. J. E. 2004, ApJ, 616, 643

Galárraga-Espinosa, D., Aghanim, N., Langer, M., & Tanimura, H. 2021a, A&A, 649, A117

Galárraga-Espinosa, D., Langer, M., & Aghanim, N. 2021b, arXiv e-prints, arXiv:2109.06198

Gheller, C. & Vazza, F. 2019, MNRAS, 486, 981

Gunn, J. E., Siegmund, W. A., Mannery, E. J., et al. 2006, AJ, 131, 2332

Hattori, S., Ota, N., Zhang, Y.-Y., Akamatsu, H., & Finoguenov, A. 2017, PASJ, 69, 39

HI4PI Collaboration, Ben Bekhti, N., Flöer, L., et al. 2016, A&A, 594, A116

Hincks, A. D., Radiconi, F., Romero, C., et al. 2022, MNRAS, 510, 3335

Ishibashi, W. & Courvoisier, T. J. L. 2010, A&A, 512, A58

Kolodzig, A., Gilfanov, M., Hütsi, G., & Sunyaev, R. 2017, MNRAS, 466, 3035

Kovács, O. E., Bogdán, Á., Smith, R. a. K., Kraft, R. P., & Forman, W. R. 2019, ApJ, 872, 83

Laigle, C., Pichon, C., Arnouts, S., et al. 2018, MNRAS, 474, 5437

Liu, A., Bulbul, E., Ghirardini, V., et al. 2021, arXiv e-prints, arXiv:2106.14518

Lumb, D. H., Warwick, R. S., Page, M., & De Luca, A. 2002, A&A, 389, 93

Malavasi, N., Aghanim, N., Douspis, M., Tanimura, H., & Bonjean, V. 2020, A&A, 642, A19

Malavasi, N., Arnouts, S., Vibert, D., et al. 2017, MNRAS, 465, 3817

Martizzi, D., Vogelsberger, M., Artale, M. C., et al. 2019, MNRAS, 486, 3766

Merloni, A., Predehl, P., Becker, W., et al. 2012, arXiv e-prints, arXiv:1209.3114

Mernier, F., Biffi, V., Yamaguchi, H., et al. 2018, Space Sci. Rev., 214, 129

Mernier, F., de Plaa, J., Kaastra, J. S., et al. 2017, A&A, 603, A80

Moutard, T., Arnouts, S., Ilbert, O., et al. 2016a, A&A, 590, A103

Moutard, T., Arnouts, S., Ilbert, O., et al. 2016b, A&A, 590, A102

Nicastro, F., Kaastra, J., Krongold, Y., et al. 2018, Nature, 558, 406

Piffaretti, R., Arnaud, M., Pratt, G. W., Pointecouteau, E., & Melin, J.-B. 2011, A&A, 534, A109

Planck Collaboration. 2016, A&A, 594, A27

Planck Collaboration. 2020, A&A, 641, A6

Planck Collaboration, Ade, P. A. R., Aghanim, N., et al. 2013, A&A, 550, A134

Predehl, P., Andritschke, R., Arefiev, V., et al. 2021, A&A, 647, A1

Predehl, P., Andritschke, R., Böhringer, H., et al. 2010, in Society of Photo-Optical Instrumentation Engineers (SPIE) Conference Series, Vol. 7732, Space Telescopes and Instrumentation 2010: Ultraviolet to Gamma Ray, 77320U

Rauch, M., Miralda-Escudé, J., Sargent, W. L. W., et al. 1997, ApJ, 489, 7

Reid, B., Ho, S., Padmanabhan, N., et al. 2016, MNRAS, 455, 1553

Rosen, S. R., Webb, N. A., Watson, M. G., et al. 2016, A&A, 590, A1

Rykoff, E. S., Roz, E., Busha, M. T., et al. 2014, ApJ, 785, 104

Schaan, E., Ferraro, S., Amodeo, S., et al. 2021, Phys. Rev. D, 103, 063513

Schneider, A., Teyssier, R., Stadel, J., et al. 2019, J. Cosmology Astropart. Phys., 2019, 020

Scoddeggio, M., Guzzo, L., Garilli, B., et al. 2018, A&A, 609, A84

Scoville, N., Abraham, R. G., Aussel, H., et al. 2007, ApJS, 172, 38

Shull, J. M., Smith, B. D., & Danforth, C. W. 2012, ApJ, 759, 23

Simons Observatory Collaboration. 2019, J. Cosmology Astropart. Phys., 2019, 056

Smith, R. K., Brickhouse, N. S., Liedahl, D. A., & Raymond, J. C. 2001, ApJ, 556, L91

Snowden, S. L., Egger, R., Freyberg, M. J., et al. 1997, ApJ, 485, 125

Snowden, S. L., McCammon, D., Burrows, D. N., & Mendenhall, J. A. 1994, ApJ, 424, 714

Sousbie, T. 2011, MNRAS, 414, 350

Sousbie, T., Pichon, C., & Kawahara, H. 2011, MNRAS, 414, 384

- Sugawara, Y., Takizawa, M., Itahana, M., et al. 2017, *PASJ*, 69, 93
- Tanimura, H., Aghanim, N., Bonjean, V., Malavasi, N., & Douspis, M. 2020a, *A&A*, 637, A41
- Tanimura, H., Aghanim, N., Bonjean, V., & Zaroubi, S. 2022, arXiv e-prints, arXiv:2201.01643
- Tanimura, H., Aghanim, N., Douspis, M., Beelen, A., & Bonjean, V. 2019a, *A&A*, 625, A67
- Tanimura, H., Aghanim, N., Kolodzig, A., Douspis, M., & Malavasi, N. 2020b, *A&A*, 643, L2
- Tanimura, H., Hinshaw, G., McCarthy, I. G., et al. 2019b, *MNRAS*, 483, 223
- Tanimura, H., Zaroubi, S., & Aghanim, N. 2021, *A&A*, 645, A112
- Tempel, E., Stoica, R. S., Martínez, V. J., et al. 2014, *MNRAS*, 438, 3465
- Tittley, E. R. & Henriksen, M. 2001, *ApJ*, 563, 673
- Ursino, E. & Galeazzi, M. 2006, *ApJ*, 652, 1085
- Weinberg, D. H., Miralda-Escudé, J., Hernquist, L., & Katz, N. 1997, *ApJ*, 490, 564
- Wen, Z. L. & Han, J. L. 2015, *ApJ*, 807, 178
- Wen, Z. L., Han, J. L., & Liu, F. S. 2012, *ApJS*, 199, 34
- Werner, N., Finoguenov, A., Kaastra, J. S., et al. 2008, *A&A*, 482, L29
- Yang, Q.-X., Xie, F.-G., Yuan, F., et al. 2015, *MNRAS*, 447, 1692
- Zeldovich, I. B., Einasto, J., & Shandarin, S. F. 1982, *Nature*, 300, 407